

Cite this: *Soft Matter*, 2012, **8**, 6320

www.rsc.org/softmatter

PAPER

Properties of short polystyrene chains confined between two gold surfaces through a combined density functional theory and classical molecular dynamics approach

Karen Johnston^{*a} and Vagelis Harmandaris^{*bc}

Received 12th March 2012, Accepted 23rd April 2012

DOI: 10.1039/c2sm25567g

The properties of atactic short-chain polystyrene films confined between two parallel gold surfaces at a temperature of 503 K are investigated using a combination of density functional theory calculations and classical atomistic simulations. A classical Morse-type potential, used to describe the interaction between the polymer and the gold surface, was parameterized based on the results of density functional calculations. Several polystyrene films were studied, with thicknesses ranging from around 1–10 nm. The structural, conformational and dynamical properties of the films were analysed and compared to the properties of the bulk polystyrene systems. The dynamics of the polystyrene close to the surface was found to be significantly slower than in the bulk.

1 Introduction

The study of model polymer nanocomposite systems, as well as general polymer–solid interfaces, at the molecular level is a very intense research area due to the development of hybrid materials, polymer coatings and lubricant films, to name a few examples. It is now accepted that the behaviour of polymer melts close to a solid surface is rather different to the bulk behaviour. For example, concerning the segmental dynamics of the macromolecules, a distribution of relaxation rates was found that depended largely on the strength of the polymer–surface interactions¹ whereas in some cases new dynamical modes appeared.²

A range of simulations have been also employed to study the effect of the interface, including dynamic Monte Carlo simulations for generic bead spring models,^{3–7} united atom molecular dynamics (MD) simulations for alkanes,⁸ atomistic MD simulations of polyolefins^{9,10} and stochastic dynamics simulations of alkanes.¹¹ Bead–spring models using dynamic Monte Carlo simulations^{5,6,12} and molecular dynamics¹³ observed that segmental packing and orientation returned to bulk values within only a couple of segment lengths from the surface and chain dimensions returned to the bulk values after 1–2 times the radius of gyration R_g .

Furthermore, some experimental studies of the glass transition temperature T_g suggest that for polymer thin films on a substrate T_g decreases with decreasing film thickness,^{14–19} while other

experimental studies report no change in T_g ^{20,21} or an increase in T_g .²² Experiments are not able to distinguish easily between the interface at the solid surface and the free surface and, therefore, the reported T_g is most likely an average value for the entire film. It is assumed that a decrease in T_g is caused by the increased mobility of the chains at the free surface. This assumption is supported by MD simulations^{8,23,24} which predict greater mobility at the free surface but a slowing down of the dynamics near a solid surface.^{3,23–26} MD simulations have also been used to measure the glass transition temperature^{27,28} but these simulations were carried out using a structureless wall potential to model the solid surface. The effect of corrugation in the surface potential is crucial, since a smooth surface potential results in faster dynamics than in bulk whereas the introduction of a site-dependence to the surface potential dramatically slows the dynamics.^{3,26}

While there is qualitative agreement on the properties of polymers at interfaces the detailed structure and dynamics also depends on the specific chemical interaction between the polymer and the surface. Many MD studies take forcefield parameters from molecule–molecule interactions and apply these to studies of molecules on surfaces, even though the chemical environment is quite different. However, to obtain quantitative information from MD simulations it is essential that the classical potential accurately describes the interaction between the specific molecule and surface of interest. In order to achieve this, a more reliable procedure is to construct classical potentials based on quantum calculations. Since it is computationally impossible to simulate a large macromolecule at a surface using quantum mechanical methods, a frequent approach is to divide the macromolecule into submolecules. This approach has been used in other systems, for example, $C_5H_7O_3$ on TiO_2 ,²⁹ polyethylene on TiO_2 ³⁰ and bisphenol-A-polycarbonate on $Ni(111)$ ³¹ and $Si(001)-(2 \times 1)$.²⁶

^aMax Planck Institute for Polymer Research, Ackermannweg 10, Mainz 55128, Germany. E-mail: johnston@mpip-mainz.mpg.de

^bDepartment of Applied Mathematics, University of Crete, GR-71409 Heraklion, Crete, Greece

^cIACM FORTH, GR-71110 Heraklion, Crete, Greece. E-mail: vagelis@tem.uoc.gr

In this paper we focus on the structural and dynamical properties of atactic short-chain polystyrene (PS) films confined between two Au(111) surfaces. To quantitatively study PS–Au systems we use a dualscale modelling approach that involves detailed density functional theory (DFT) calculations and classical MD simulations of PS–Au systems. Au(111) has a well-defined surface structure, compared to substrates such as silica, which makes it easier to understand the interaction between the polymer and the surface. The interaction of one styrene monomer with gold is assumed to be well represented by the interactions of its two components (benzene and ethane) with gold. Parameters of the atomistic pair potentials for the surface interaction are obtained by fitting the classical molecule–surface interaction to the equivalent interaction calculated using DFT with van der Waals forces. The development of a classical surface potential based on the DFT results is described and the accuracies of Lennard-Jones and Morse potentials are compared. For the benzene–gold interaction we use previously parameterised Morse potentials.³² Finally, the properties of atactic styrene oligomer films of different thicknesses confined between two parallel gold surfaces are investigated.

In the next section we describe the methodology giving some details about the DFT calculations as well as the classical atomistic MD simulations. In section 3 we present results from the DFT calculations of ethane on the Au(111) surface. The new PS–Au classical force field, derived through an optimization procedure of the DFT data, as well as the analysis of the density, structure and dynamics of various PS–Au systems are also presented. Finally, our findings and conclusions are summarized in Section 4.

2 Method

Density functional theory (DFT) calculations were performed using the VASP code,^{33–36} which employs a plane wave basis set to describe the valence electrons. A plane wave cutoff energy of 400 eV was chosen and projected augmented waves were used to describe the core electrons.^{37,38} van der Waals interactions were included *via* a self-consistent implementation of the vdW-DF functional^{39–41} with PBE exchange.^{42,43} The calculated lattice constant of bulk, fcc Au was 0.423 nm, which overestimates the experimental one of $a_0 = 0.408$ nm by less than 4%. For the adsorption calculations, the surface was 4×4 times the surface unit cell, which was sufficient to avoid any interaction between the molecule and its periodic image. The slab was four-atomic layers deep, with the bottom two layers held fixed. A Brillouin zone mesh of $4 \times 4 \times 1$ was used (equivalent to $16 \times 16 \times 1$ for a surface unit cell). The relaxations were terminated when the maximum force on any atom was less than 10 meV \AA^{-1} .

The classical atomistic MD *NPT* simulations were performed using the GROMACS code.^{44–46} The pressure was maintained at $P = 1$ atm using a Berendsen barostat. The stochastic velocity rescaling⁴⁷ thermostat was used to keep $T = 503$ K. A time step of 0.001 ps was used. In the classical simulations the surface is represented by an array of fixed particles placed in the ideal positions of bulk gold. For the classical simulations the experimental lattice constant, $a_0 = 0.408$ nm, of gold at $T = 300$ K was used. This is a rather good assumption since gold has a very small thermal expansion and only increases to 0.410 nm at $T = 618$ K.⁴⁸

Furthermore, using this value for the Au lattice constant keeps the current ethane–gold potential consistent with the previously developed forcefield for benzene–gold. Periodic boundary conditions were used in all directions so that the PS also interacts with the bottom of the gold surface in the image cells. For the slab calculations the electrostatics are calculated using the Particle–Mesh Ewald method with a force and potential correction to avoid interactions between slab images in the z -direction. The dispersion cutoff length was 1.0 nm and the dispersion correction for the polymer–polymer interaction, as well as the pressure was used. We should note here that the applied dispersion correction assumes that the system is homogeneous, *i.e.* does not take into account the non-uniform density profile of the polymer–solid interfacial systems (see Appendix of ref. 49). To check for the error introduced we performed test runs with a larger cutoff length of 1.4 nm and the error in the density, as well as in the dynamics, of the hybrid systems appears to be small, less than 5%. A 7-atomic-layer slab with a thickness of about 1.65 nm was used, which is thicker than the cutoff length. The atomistic force field parameters for PS were taken from the literature⁵⁰ and arithmetic combination rules were used. The reference bulk PS system consists of 50 10-monomer chains in a cubic box. The force field between the phenylene C and H atoms and gold was taken from a study of benzene on gold³² and the force field for the C and H backbone atoms is obtained from the analysis of the DFT calculations as described below.

Four films, denoted S1 to S4, with different numbers of chains, N , were prepared. The chains were all 10 monomers long ($M_w = 1040 \text{ g mol}^{-1}$) and each chain has a random tacticity. For the thicker films, S3 and S4, the lateral dimension of the surface is 4.616 nm, corresponding to 16×16 surface unit cells along the a and b directions (see Fig. 1). For the thinnest two films the surface was doubled in the a and b directions (32×32 surface unit cells) to improve statistics.

The PS–Au systems were set up and equilibrated as follows. First, chains with different tacticities were set up in an hexagonal box with a gold slab and run with pressure coupling in the z -direction at 1 atm. The systems were equilibrated by running at a high temperature T_{equil} for 10 ns after which the end-to-end vector is decorrelated. This was followed by cooling to the target temperature of 503 K, which is over 150 K above the bulk experimental value of 10-mer PS, which has been measured in the range $T_g = 279\text{--}328$ K.^{51–53} Cooling rates of $10\text{--}300 \text{ K ns}^{-1}$ were tested and the dependence of the properties on the cooling rate was checked. Afterwards, a cooling rate of $25\text{--}30 \text{ K ns}^{-1}$ was chosen and once the temperature reached 503 K the system was run for some extra time (about 5–10 ns) before statistics were taken. Finally, after equilibration, production runs of 100 ns duration were performed. The equilibration temperatures, T_{equil} , and cooling rates, τ , are given in Table 1. For the smallest system three independent films were prepared in order to study the dependence on the history of the sample (setup of the model system).

3 Results and discussion

In this section we present results about the confined PS systems from the detailed DFT calculations and the classical atomistic simulations.

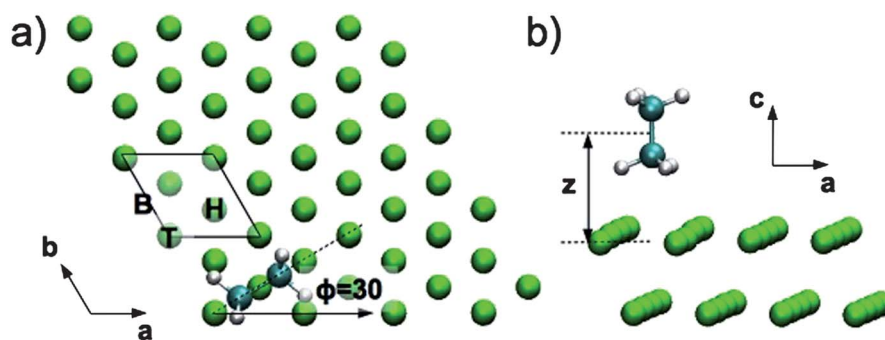


Fig. 1 (a) The Au(111) surface showing an ethane molecule on a hollow site, H, oriented with angle $\theta = 0$ (C–C bond flat on the surface) and $\phi = 30$ (angle between the C–C bond and the a -axis). The T, B and H show where the centre of the molecule would be for the top, bridge and hollow site, respectively. A surface unit cell has been highlighted. (b) The ethane molecule on the H site with $\theta = 90$. z is defined as the distance (perpendicular to the surface) between the mid-point of the C atoms and the ideal position of the top Au atoms.

Table 1 Setup and equilibration details for the four films

System	N	T_{equil} (K)	τ (K ns ⁻¹)
S1A	40	1200	25
S1B	40	1200	25
S1C	40	1200	25
S2	80	1000	25
S3	50	800	30
S4	100	800	30

3.1 Density functional theory

The main usage of the DFT calculations is to study the (single) monomer–surface interaction and also to derive an accurate and reliable classical atomistic force field for the molecule(PS)–surface(Au) interaction. As mentioned in the introduction, the interaction of one styrene monomer with gold is assumed to be well represented by the interactions of its two components (benzene and ethane) with gold. Parameters for the benzene–Au interaction are taken from a previous parametrization of DFT calculations.³² Here we calculate parameters for the ethane–Au interaction.

There are three adsorption sites for ethane on the Au(111) surface, namely, the top site (T), the bridge site (B), and the hollow site (H)[†] as shown in Fig. 1. In order to study the (many) possible orientations for ethane on the surface we define θ as the angle that the C–C bond makes with the surface plane and we refer to orientations with $\theta = 0$ as flat and with $\theta = 90$ as vertical. For the flat orientations, ϕ is the angle between the C–C bond and the crystallographic a axis as shown in Fig. 1. We define the adsorption energy as $E_{\text{ads}} = E_{\text{tot}} - E_{\text{slab}} - E_{\text{mol}}$ where E_{tot} , E_{mol} and E_{slab} are the total energies of the whole system, the ethane molecule and the gold surface slabs, respectively. The distance, z , is defined to be the perpendicular distance from the ideal position of the top Au atomic layer to the midpoint of the carbon atoms of the ethane molecule (see Fig. 1b).

The equilibrium adsorption energies and angles for each site and various orientations are shown in Table 2. The ground state

configuration is on the hollow site with $\theta = 0^\circ$, $z_{\text{eq}} = 0.351$ nm and an equilibrium adsorption energy of 35.7 kJ mol⁻¹. The dependence on the adsorption site is weak with differences in adsorption energy of about 2–3%, which is similar to the behaviour observed for benzene on Au(111).³² In contrast there are clear differences between the adsorption energies of the different molecule orientations *i.e.* E_{ads} of the vertical configurations ($\theta = 90^\circ$) is about 20% less than the flat ones for all sites. However, the dependence on the in-plane angle ϕ is very weak.

The interaction between ethane and gold surfaces is mostly due to van der Waals forces. If we calculate the ground state structure using the PBE exchange and correlation functional, which does not account for vdW forces, using the corresponding PBE equilibrium gold lattice constant of 0.417 nm, then the adsorption energy is only 9.6 kJ mol⁻¹. It is only recently that accurate vdW functionals for DFT calculations have been developed^{39,40} and there are very few studies of the interaction between ethane and gold. However, similar behaviour is also seen for other molecules that do not form strong chemical bonds with a surface as, for example, benzene adsorbed on gold³² or on graphene.⁵⁴ As far as we are aware, there is only one experimental study for the adsorption energy of ethane on gold, which found an adsorption energy (or activation energy of desorption) of 24.1 kJ mol⁻¹ using helium atom reflectivity.⁵⁵ Our calculations give a larger adsorption energy than experiment, which has been also observed for benzene–Au.³² The cause of such discrepancies between the DFT calculations and experimental data are related with uncertainties at the DFT level (mainly the choice of exchange functional) as well as with the experimental

Table 2 Adsorption sites, angles, distances and energies for ethane with 0.0625 ML coverage

Site	$\theta/^\circ$	$\phi/^\circ$	z_{eq} (nm)	E_{ads} (kJ mol ⁻¹)
H	0	0	0.351	-35.7
H	0	30	0.351	-35.7
H	90	0	0.410	-28.9
H	90	30	0.410	-28.0
T	0	0	0.366	-34.7
T	90	0	0.425	-27.0
B	0	0	0.351	-34.7
B	90	0	0.410	-28.0

[†] There are two hollow sites on Au(111), namely fcc and hcp, but since the difference in energy between them is so small we will just refer to them as the hollow site.

uncertainties related to deviations from a perfect crystal, such as surface roughness, impurities, *etc.*

3.2 Classical force field for the PS–Au interaction

A major part of the current work concerns the development of an accurate force field for the polymer–surface interaction. This is of particular importance since the strength of the adhesive energy determines the properties of the hybrid interfacial system. A standard approach in many classical simulations, is to use force fields for surface interactions that were parametrized for the bulk material rather than interfacial systems or that used DFT calculations that neglected vdW forces. However, as shown in the previous subsection, the vdW forces are substantial and should not be ignored for typical polymer–solid systems, including the PS–Au system studied here. Thus, in order to develop an accurate classical force field, we use the data from the DFT calculations presented in the previous section. In more detail we try to obtain, through an optimization procedure, a set of classical atomistic non-bonded pair parameters that describe *all* available DFT data. Note that this approach has been successfully used for describing benzene–Au systems.³²

As mentioned above, for the classical simulations we use a detailed model in which all surface Au atoms are presented explicitly. Then, we obtain pair potentials for the molecule–surface interaction (in our case Au–C and Au–H) using the detailed DFT data. Different functional forms can be used for the classical pair intermolecular potentials and in this work we considered two of them. The first is the Lennard-Jones pair potential

$$V_{\text{LJ}}(r_{ij}) = 4\varepsilon_{ij} \left\{ \left(\frac{\sigma_{ij}}{r_{ij}} \right)^{12} - \left(\frac{\sigma_{ij}}{r_{ij}} \right)^6 \right\} \quad (1)$$

which has two adjustable parameters, ε_{ij} and σ_{ij} , per atom pair. The second is a more detailed Morse-type pair potential of the form

$$V_{\text{M}}(r_{ij}) = \varepsilon_{ij} \{ \exp[-2\alpha_{ij}(r_{ij} - r_{0ij})] - 2\exp[-\alpha_{ij}(r_{ij} - r_{0ij})] \} \quad (2)$$

which has three adjustable parameters, ε_{ij} , r_{0ij} and α_{ij} , per atom pair, where the parameter α determines the shape/width of the potential. For both potentials the indices i and j denote the atom types (in this case i is an Au atom and j is a C or H atom).

Our goal is to find the set of non-bonded parameters that best describe all the available DFT data, *i.e.* molecule–surface interaction energies for different adsorption sites, molecule orientations and over a suitable range of molecule–surface distances, z . This is a complicated numerical problem, since it involves fitting over a many-parameter space without a clear global minimum. To achieve this we use an optimization algorithm, which is based on simulated annealing. In this scheme the parameters of the molecule–surface non-bonded interaction are determined iteratively (starting from an initial guess) in order to minimize a target-cost function. The cost function is defined as the difference between the quantum and classical molecule–surface interaction energies, for all distances and all different configurations (various adsorption sites and orientations). Different weights to distinguish the importance of the data points in the

optimization procedure can be used. More details about the optimization scheme can be found elsewhere.³²

A PS monomer consists of C and H backbone atoms as well as C and H atoms of the phenylene group, as shown in Fig. 1c. For the latter we use the force field developed previously for describing benzene–gold systems.³² For the former, we use the DFT data obtained for ethane (see previous section) to develop new ethane–gold surface potentials, in a similar procedure as used for benzene on gold. The fitting procedure uses the data for all three sites, H, B and T, with both flat and vertical orientations. Since the dependence on ϕ is negligible we only considered orientations with $\phi = 0$. In Fig. 2 the DFT data for the various molecule orientations (squares for the flat and circles for the vertical ones) as well as the results from the classical pair potentials (lines), taken from the optimization procedure described above, are shown. Optimised parameters for the pair atomistic interactions are given in Table 3.

First, in Fig. 2a we present classical molecule–surface interactions using the standard LJ potentials compared to DFT. The classical data (full lines) are obtained by parameterizing each adsorption site, for the flat configurations, independently since it is not possible to find a set of LJ parameters that describe all the DFT minima simultaneously. Furthermore, during the optimization procedure larger weights were given for data points close to the minimum of energy because it is also not possible to find a set of parameters that fit all the points (different molecule–surface distances) for a specific configuration. As we can see the classical interaction at the minima and longer distances are in a rather good agreement with the DFT data, whereas the shape of the interaction curve is too steep at low values of z . To check the transferability of the obtained classical potential parameters we use them to calculate the molecule–surface interaction energy of the

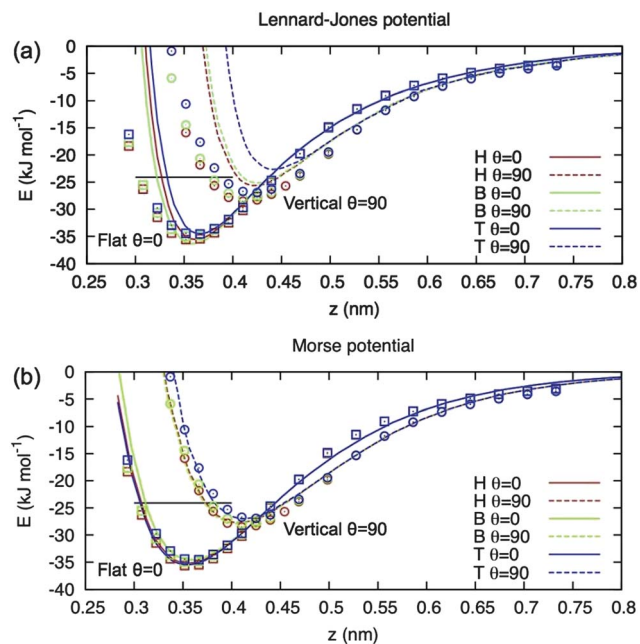


Fig. 2 Adsorption energy as a function of the distance from the surface. The DFT results (symbols) are compared to the results from the pair potentials (lines), obtained from the optimization procedure using (a) Lennard-Jones and (b) Morse non-bonded potentials.

Table 3 Force field parameters for the interaction of PS with the Au(111) surface. The parameters for the phenylene atoms were taken from ref. 32

Type	Atom pair	$\sigma, r_0/\text{nm}$	$\epsilon/\text{kJ mol}^{-1}$	α/nm^{-1}
LJ	Au-C _{ethyl}	0.37	1.95	—
LJ	Au-H _{ethyl}	0.25	0.16	—
Morse	Au-C _{ethyl}	0.42	0.95	12.06
Morse	Au-H _{ethyl}	0.38	0.42	9.74
Morse ³²	Au-C _{phenyl}	0.41	0.93	10.14
Morse ³²	Au-H _{phenyl}	0.40	0.31	11.66

vertical configurations (dashed lines in Fig. 2a). It is also clear that there are strong deviations between the derived classical energies and the DFT data in all but the large molecule–surface distances. The reason for these discrepancies is most probably due to the very steep form of the repulsive part (12th power) of the LJ potential, which is not suitable for describing the complex short-range quantum behaviour of the molecule–surface system.

In the second parameterization we have used a non-bonded Morse-type potential for the classical pair C–Au and H–Au interaction. We fit simultaneously both the flat and the vertical molecule orientations. Results are shown in Fig. 2b. In contrast to the LJ data discussed above, the optimization scheme using the Morse potential (data in Fig. 2b) works much better; *i.e.* one set of parameters for atomistic classical simulations can accurately describe the DFT data for *all* different molecule orientations and molecule–surface distances studied here. It is also interesting to note the very good agreement between the classical and the DFT data even for very short molecule–surface distances, where there are small displacements of the Au atoms from their ideal positions (see Fig. 1b), which are not described at the classical level.

In summary, it is clear that a classical atomistic pair parameterization of the PS–Au interaction using a Morse-type potential is better than the Lennard-Jones one in describing the DFT data. Finally, we should also state that a Lennard-Jones potential was previously used to describe the interaction between organic molecules and surfaces by fitting to DFT and second-order Møller–Plesset calculations.⁵⁶ However, no direct comparison between the *ab initio* results and the Lennard-Jones potentials was presented. Our data show that typical LJ pair potentials for the molecule–surface interaction cannot accurately describe the DFT data for the whole range of molecule–surface distances.

3.3 Confined polystyrene films

In this section we present results from classical atomistic MD simulations of PS confined systems, using the new PS–Au atomistic interaction developed in the previous section. We have simulated four different systems, S1–S4, (see Table 1) with 40, 80, 50 and 100 PS oligomers, respectively, between two parallel Au(111) surfaces. For the smallest system, which is the most strongly confined, we have performed three independent simulations, to check the dependence on setup and history of the samples. In all cases $T = 503$ K and $P = 1$ atm. In Fig. 3 we present typical snapshots, taken from the MD simulations, for each film. From these snapshots a PS adsorption layer can be seen at the Au surfaces for all systems.

3.3.1 Structural properties. Various properties of the different systems, including film thickness, d , density, ρ , average end-to-end distance, $\langle R_c^2 \rangle^{\frac{1}{2}}$, and radius of gyration, $\langle R_g^2 \rangle^{\frac{1}{2}}$, are presented in Table 4. The film thicknesses were calculated by subtracting the thickness of the 7-atomic-layer gold slab (where the interlayer spacing of Au(111) is $a_0/\sqrt{3} = 0.236$ nm) from the average box length along the z -direction. The average film thicknesses of the four model systems are approximately 0.96 nm, 1.9 nm, 4.7 nm and 9.5 nm, which correspond to about 0.62, 1.2, 3.1 and 6.2 times the average end-to-end distance ($\langle R_c^2 \rangle^{\frac{1}{2}} = 1.54$ nm) of 10-mer bulk PS, respectively. The average density in each case is higher than the bulk density, which is due to the denser adsorption layer at the gold surface. It is clear that $\langle R_c^2 \rangle^{\frac{1}{2}}$ of PS chains for all but the thinnest films have values which are very close to the bulk one. The components of R_g parallel and perpendicular to the surface are also shown in Table 4. For the S1 and S2 systems the chains are orientated parallel to the surface but only in S1 do the chains appear to be compressed with a smaller R_g than bulk. All three S1 films are under particularly strong confinement since their thickness is smaller than the bulk value of $\langle R_c^2 \rangle^{\frac{1}{2}}$. Consequently $\langle R_g^2 \rangle^{\frac{1}{2}}$ and, more noticeably, $\langle R_c^2 \rangle^{\frac{1}{2}}$ are smaller in these films. Although the density and value of $\langle R_c^2 \rangle^{\frac{1}{2}}$ is similar in each S1 film, the value of $\langle R_g^2 \rangle^{\frac{1}{2}}$ is less uniform.

To further study the fluctuations of the end-to-end distance, we show in Fig. 4 the time evolution of the root mean square $R_c(t)$ for all systems. We see that for all but the thinnest system (S1), the average value of the end-to-end distance of the PS chains is very close to the value of the unperturbed bulk system. Small differences between the different systems are practically within error bars. In contrast, all the S1 films have smaller end-to-end distances and smaller fluctuations than the larger films. Furthermore, the three different S1 films also have different values and, clearly, for this system, the results depend on the equilibration–annealing period (history of the sample). This is due to the fact that these strongly confined films are effectively frozen and their structures are rather dependent on set up and history, as will be shown later. The running average data show that during the simulation runs the root mean square R_c reach steady-state, time-independent values. The behaviour of the radius of gyration is qualitatively similar. Note that this analysis is over the entire confined polymer system. The variation of the chain dimensions along z , are studied in the next subsection.

The molecular density profiles, $\rho(z)$, of S3 and S4 are displayed in Fig. 5a. The densities are based on the monomer centre-of-mass and are time-averaged. In these *NPT* simulations the box size along the c -axis fluctuates and, therefore, the analysis has been performed using fractional coordinates (units of the box length) and then finally multiplying the fractional coordinates by the average box length. As expected, the density profiles are symmetrical with respect to the centre of the film. As seen in the snapshots of the atomistic simulations in Fig. 3, all films show a dense layer around 0.4 nm from the gold surface, labelled I. For the S3 and S4 systems the density profile exhibits a weak second peak, labelled II, at a distance of around 1 nm from the Au surface. Similar density profiles with a characteristic oscillation have been observed in past simulations of polymer–solid

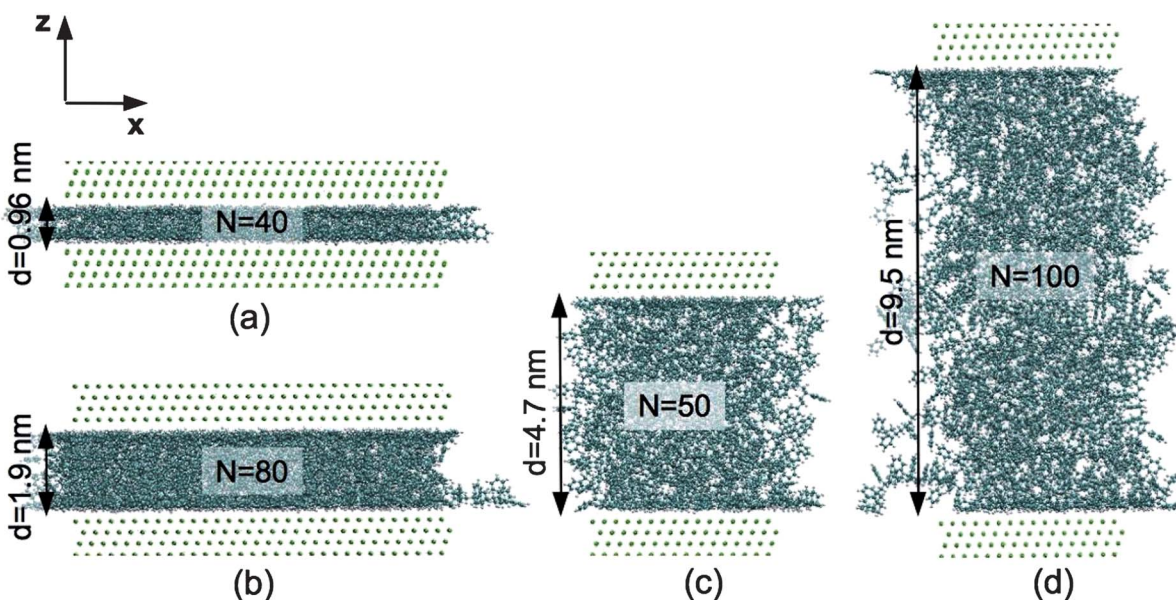


Fig. 3 Snapshots for the four systems (periodic boundary conditions applied on the molecule center-of-mass) studied (a) S1 with 40 chains, (b) S2 with 80 chains, (c) S3 with 50 chains and (d) S4 with 100 chains. Systems S1 and S2 appear to be more dense but this is because the simulation cells are doubled along the x and y directions to improve statistics.

interfaces with atomistic^{8,30,49,57} as well as coarse-grained bead-spring models.¹¹ In the middle region of systems S3 and S4, at distances beyond about 1.5–2 nm from the Au surfaces, ρ assumes an approximately constant value equal to the density of the bulk PS 10-mer melt, $\rho = 0.97 \text{ g cm}^{-3}$. In Fig. 5b a close-up of the density profiles of all systems is presented. All three independent S1 films are shown. Similar to S3, the S2 system shows one PS layer at the Au surface and the density in the middle of the film is very close to the bulk value. In contrast, the S1 films exhibit a qualitatively different behaviour with two strong adsorption layers and no bulk-like region.

3.3.2 Conformational properties. In this subsection, we first present data on segmental level ordering by analysing the local bond orientation tendencies induced by the Au surfaces. In general, the orientation of a molecule can be quantified by calculating the second rank order parameter. For an arbitrary vector along the molecule, \mathbf{v} , this is defined as

$$P_2(\cos(\theta)) = \frac{3}{2} \langle \cos^2 \theta \rangle - \frac{1}{2} \quad (3)$$

Table 4 Properties of the four systems S1–S4, including three independent simulations of system S1 and the bulk (B) values. ρ is the film density, d is the thickness, R_e is the end-to-end distance, R_g is the radius of gyration and R_{gz}^2 and R_{par}^2 are its components perpendicular and parallel to the surface, respectively

Film	N	d/nm	$\rho/\text{g cm}^{-3}$	$\langle R_e^2 \rangle^{1/2}/\text{nm}$	$\langle R_g^2 \rangle^{1/2}/\text{nm}$	$\langle R_{gz}^2 \rangle/\text{nm}^2$	$\langle R_{par}^2 \rangle/\text{nm}^2$
S1A	40	0.96	0.98	1.41	0.66	0.05	0.20
S1B	40	0.96	0.98	1.31	0.65	0.05	0.19
S1C	40	0.96	0.97	1.37	0.66	0.05	0.19
S2	80	1.89	1.00	1.59	0.69	0.08	0.20
S3	50	4.73	0.99	1.58	0.69	0.13	0.17
S4	100	9.54	0.98	1.54	0.69	0.13	0.17
B	50	—	0.97	1.54	0.69	0.16	0.16

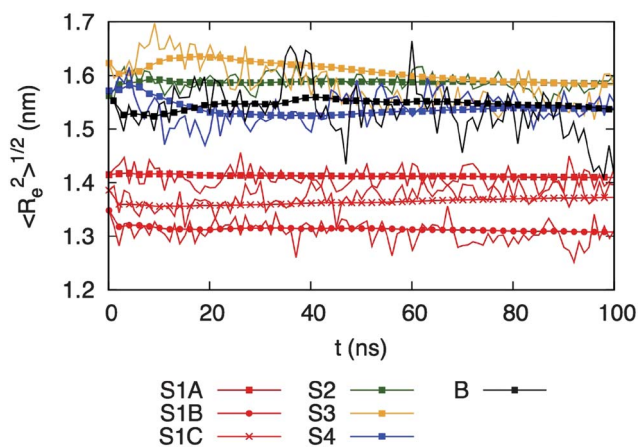


Fig. 4 Time evolution of the end-to-end distance of the PS chains of all systems studied here. The instantaneous values $R_e(t)$ are shown with lines whereas the running average data is shown with symbols.

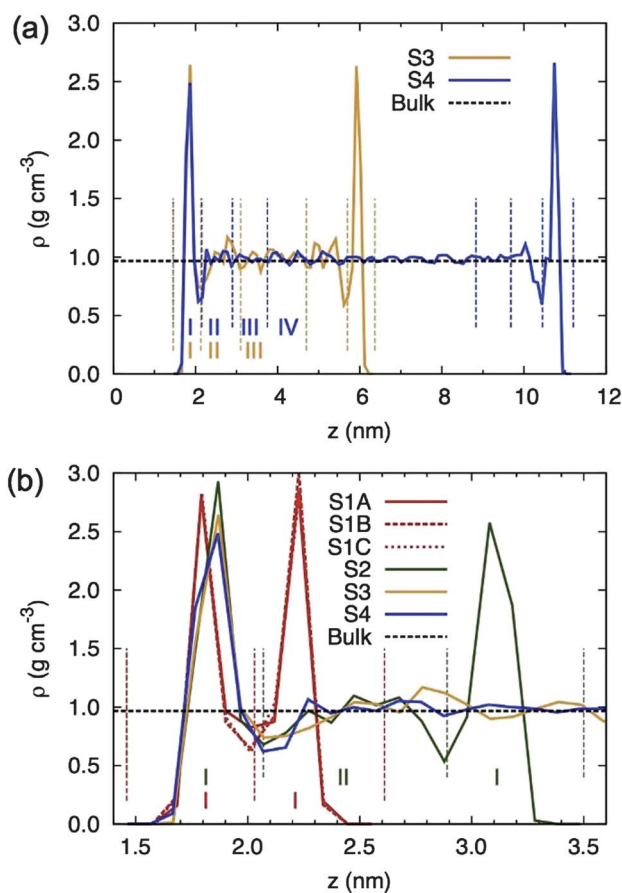


Fig. 5 a) Monomer density for the S3 and S4 systems along the z -direction. b) Close-up of the four systems, including the three independent S1 films. In both graphs the vertical dashed lines correspond to the adsorption layer boundaries used in the analysis.

where θ is the angle of the vector \mathbf{v} with the z coordinate axis (in this case normal to the surface). The brackets denote the ensemble average of all molecules in the system. The limiting P_2 values of -0.5 and 1.0 correspond to molecules oriented parallel and perpendicular to the surface, respectively. A value of 0.0 means that the molecules are randomly oriented.

We would like to distinguish between the local orientation of the backbone chains and of the side (phenyl) groups. Therefore, we analyze the local-bond orientation of the PS monomer by choosing vectors that connect a pair of carbons either at opposite sides of the phenyl ring or in the neighbouring monomers along the backbone, as shown in Fig. 6. Within the phenyl group there is a choice of three such atom pairs, of which only two are equivalent. The vector that includes the carbon atom attached to the backbone, $\mathbf{v}^{\text{ph}b}$, is not equivalent by symmetry to the other two vectors, $\mathbf{v}^{\text{ph}p}$. Similarly for the backbone chain there are two choices of atom pairs: those connected to the phenyl group, $\mathbf{v}^{\text{pb}p}$, and those that are not, $\mathbf{v}^{\text{bb}b}$.

Graphs showing the variation along z of the bond order parameters are shown in Fig. 7. The data is analysed along the direction of confinement, z , by dividing the space into bins separated by parallel x - y planes, and then averaged to take into account the symmetry of the film. For all the vectors and systems, the bond order parameters attain negative values of almost -0.5

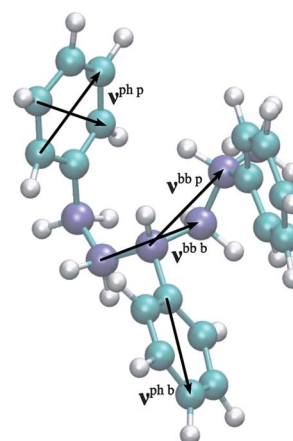


Fig. 6 A PS 3-mer chain, with the backbone C atoms highlighted in lilac for clarity and showing the vectors used for bond order analysis.

at around 0.1 – 0.2 nm away from the Au surfaces, indicating the strong tendency of the backbone and phenyl groups to orient parallel to the surface plane. The P_2 then increase to a peak at ≈ 0.3 – 0.5 nm from the surface, although the height and position depends on the vector and system under consideration. For systems S2–S4 the bond order parameter is zero in the centre of the film, indicating random orientation, whereas in system S1 the parameters do not reach a constant zero value in the centre. Despite the differences in the chain dimensions of the three S1 systems, there is little difference in average local bond orientation in the films.

For the order parameter of the phenyl vector connected to the backbone chain, $P_2^{\text{ph}p}$, systems S2–S4 have a peak value of 0.4 – 0.5 , around 0.5 nm from the surface (distance of about 2.0 nm), shown in Fig. 7a. This peak corresponds to the position of the first minimum in the density profile *i.e.* the end of the first adsorption layer. The other phenyl order parameter, $P_2^{\text{ph}b}$, is shown in Fig. 7b, and the peak is shifted towards the surface by around 0.2 – 0.3 nm. This shows that $\mathbf{v}^{\text{ph}p}$ has a slightly more random orientation close to the surface than $\mathbf{v}^{\text{ph}b}$. This is a consequence of the fact that the $\mathbf{v}^{\text{ph}p}$ are allowed to tilt around the $\mathbf{v}^{\text{ph}b}$ ‘axis’, whereas $\mathbf{v}^{\text{ph}b}$ is constrained by the backbone. An analogous behaviour is seen for $P_2^{\text{pb}p}$ and $P_2^{\text{bb}b}$, shown in Fig. 7c and d, respectively. By comparing $P_2^{\text{ph}p}$ and $P_2^{\text{ph}b}$ in Fig. 7a and c, it is clear that the backbone peak value is higher than that of the phenyl vector, particularly in the case of the S1 films. This means that the orientation of the backbone is more strongly aligned perpendicularly to the surface at the density minimum.

It is easier to understand more about the orientational ordering by looking at the average values of the order parameters in the adsorption layers, which are defined as the distance between two consecutive minima in the density profiles and are labelled I, II, *etc.*, in Fig. 5. The data are shown in Table 5. The order parameter $P_{2\text{ads}}^{\text{ph}b}$ of the first adsorbed layer, is negative for all systems, showing the tendency of molecules to be parallel to the surface plane. It is clear that this tendency is stronger in the S1–S3 systems with values of $P_{2\text{ads}}^{\text{ph}b}$ between -0.25 and -0.33 . The S4 system has a lower value of $P_{2\text{ads}}^{\text{ph}b}$ than the other systems, indicating that it is slightly less ordered than the other systems. This is probably due to the larger fluctuations and faster

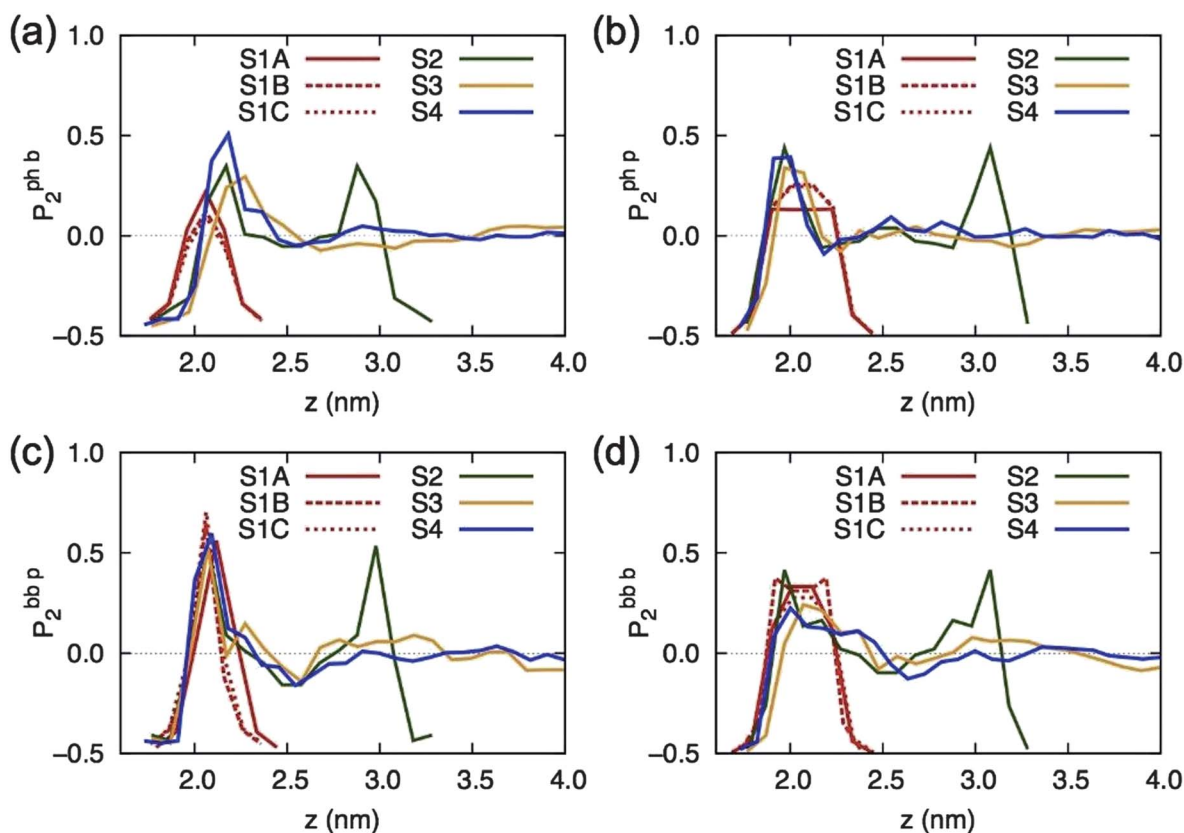


Fig. 7 The variation of the bond order parameter with distance from the surface for all systems. The graphs correspond to the vectors (a) $\mathbf{v}^{\text{ph } b}$, (b) $\mathbf{v}^{\text{ph } p}$, (c) $\mathbf{v}^{\text{bb } p}$, and (d) $\mathbf{v}^{\text{bb } b}$, as shown in Fig. 6.

dynamics, as seen in Fig. 4 in the previous subsection. In addition, the thinner films feel the influence of both interfaces, so the orientation is more strongly affected. The bond order parameters in regions II, III and IV in S2–S4 were also analysed but the magnitudes of all the order parameters are less than 0.1 indicating weak or random ordering. The analysis of $\mathbf{v}_{\text{ads}}^{\text{ph } p}$ shows a clear difference between the most confined films S1A–C and the other films S2–S4. For the S1 films the vectors have a slight tendency to be parallel to the surface, whereas in the larger systems they show a weak preference for vertical orientation. Both backbone bond order parameters $P_{2 \text{ ads}}^{\text{ph } p}$ and $P_{2 \text{ ads}}^{\text{bb } b}$ are

Table 5 Average value of the P_2 bond order parameters in the adsorption layer of each film for the vectors shown in Fig. 6. Error bars are for all points about 0.05

Film	Region	$P_{2 \text{ ads}}^{\text{ph } b}$	$P_{2 \text{ ads}}^{\text{ph } p}$	$P_{2 \text{ ads}}^{\text{bb } p}$	$P_{2 \text{ ads}}^{\text{bb } b}$
S1A	I	-0.26	-0.10	-0.17	-0.06
S1B	I	-0.28	-0.09	-0.16	-0.03
S1C	I	-0.29	-0.08	-0.15	-0.05
S2	I	-0.33	+0.08	-0.27	-0.22
	II	+0.09	-0.01	-0.02	-0.02
S3	I	-0.25	+0.10	-0.28	-0.22
	II	+0.02	-0.01	+0.01	+0.02
	III	+0.02	+0.01	-0.01	-0.02
S4	I	-0.20	+0.08	-0.32	-0.28
	II	+0.06	+0.02	-0.06	-0.05
	III	+0.01	+0.01	0.00	0.00
	IV	0.00	0.00	-0.01	-0.01

negative for all systems, again showing the tendency of molecules in the first adsorption layer to be parallel to the gold surface. The larger systems S2–S4 have more strongly negative values than S1A–C films. In particular, the orientation of the bond vector $\mathbf{v}_{\text{ads}}^{\text{bb } b}$ is almost random in the S1 films but has quite a strong parallel orientation in S2–S4.

Next, we show information about the conformational properties of PS at the level of the entire chain. Changes in the shape of the chains can be analyzed in terms of a global descriptor of the overall polymer melt configuration, the so-called conformation tensor \mathbf{C} . This is defined as the second moment tensor of the end-to-end distance vector, \mathbf{R}_e , of a polymer chain divided by one-third of its unperturbed mean-square end-to-end distance, $\langle R_e^2 \rangle_0$, averaged over all chains in the system

$$\mathbf{C}_{\alpha\beta} = 3 \left\langle \frac{\mathbf{R}_{e\alpha} \mathbf{R}_{e\beta}}{\langle R_e^2 \rangle_0} \right\rangle \quad (4)$$

where α and β are the x , y and z components. The conformation tensor \mathbf{C} is equal to the identity tensor, $\mathbf{C} = \mathbf{I}$, for any isotropic polymer system at equilibrium. However, when the polymeric chains are near to a boundary region, or there is a strong flow field in the system, the shape of the macromolecular chains is distorted and \mathbf{C} departs from its equilibrium value. In such a case, the non-zero components of \mathbf{C} provide a measure of the orientation and/or extension of the chains.

The conformation tensor components, \mathbf{C}_{xx} , \mathbf{C}_{yy} and \mathbf{C}_{zz} , were analysed as a function of the distance from the surface. The film

was divided into layers along z , approximately 1 nm thick, and within each layer, \mathbf{C} is obtained as an ensemble average of individual molecular conformation tensors over chains whose centers-of-mass lie in that layer. The results are then symmetrized along the z -axis and the two in-plane components are averaged. Fig. 8 displays the effect of the gold surface on the in-plane and perpendicular components for the S2–S4 systems. In all cases the in-plane components, $C_{\text{par}} = \frac{1}{2}(C_{xx} + C_{yy})$ are larger than 1.0 at the surface whereas the zz components are smaller. Therefore, the conformations are compressed along the z -direction and elongated along the surface plane, which means that the chains are lying along the surface. Quantitatively, $C_{zz} \approx 0.2$, which means that the surface affects the perpendicular component more than the in-plane components. A similar behavior has been also observed from computer simulations of alkanes near solid surfaces.^{4,49,58} It can be also seen from the S4 film that the conformation returns to the bulk value of 1.0 at around 1–2 nm from the Au surface, which is of the order of the average bulk end-to-end distance of 1.54 nm.

To further quantify these results and compare the various systems, the conformation tensor components of the adsorption

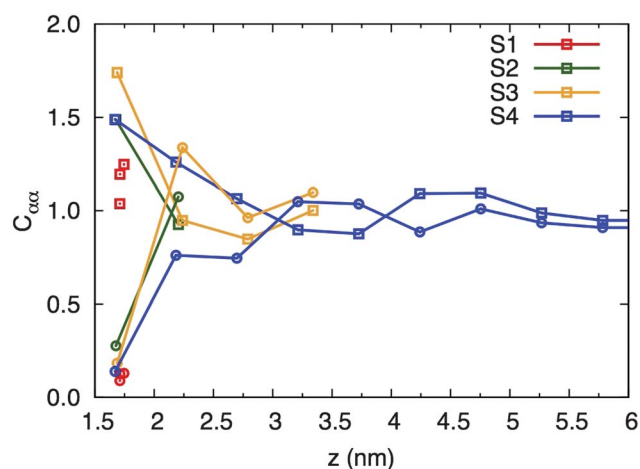


Fig. 8 Variation of the conformation tensor components, C_{xx} , C_{yy} and C_{zz} , with z for all systems. Squares show the components averaged in the surface (xy) plane and circles show the components perpendicular to the surface.

Table 6 Average value of the conformation tensors in the different regions of each film as labelled in Fig. 5. $C_{\text{par ads}}$ is the average in-plane value. Error bars are estimated to be about 10–20%

Film	Region	$C_{\text{par ads}}$	$C_{zz \text{ ads}}$
S1A	I	1.27	0.14
S1B	I	1.10	0.09
S1C	I	1.25	0.13
S2	I	2.12	0.21
	II	0.94	0.69
S3	I	1.77	0.14
	II	0.91	1.13
	III	0.96	1.14
S4	I	1.52	0.11
	II	1.18	0.72
	III	0.97	1.00
	IV	1.01	0.95

layers for each system are given in Table 6. S3 and S2 exhibit similar conformational properties as S4. For the S1 films the results are more varied which is, again, a consequence of the dependence on system setup and the slow dynamics of these systems, which will be discussed in the next section. We should also note that the studied systems show a clear uniaxial anisotropy, studied through the Saupe matrix, \mathbf{S} , (data not shown here) of the PS molecules along the z -direction.

3.3.3 Dynamical properties. In this section the effect of the confinement on the dynamics of the PS–Au films is analysed and discussed. The dynamics of the PS oligomers is studied both at the monomer level, through properly defined orientational relaxation functions, and at the whole molecule level through the time evolution of the center-of-mass mean square displacements and diffusion coefficients.

The local orientational dynamics of a molecule can be studied through the time correlation functions of a vector \mathbf{v} . In more detail, we consider the relaxation of the second-order bond order parameter P_2 defined as:

$$P_2(t) = \frac{3}{2} \langle \cos^2(\theta(t)) \rangle - \frac{1}{2} \quad (5)$$

where θ is the angle of the vector time t relative to its original position. As before, we consider the vectors $\mathbf{v}^{\text{ph p}}$, $\mathbf{v}^{\text{ph b}}$, $\mathbf{v}^{\text{bb p}}$, and $\mathbf{v}^{\text{bb b}}$ discussed in the previous subsection and shown in Fig. 6. The time autocorrelation function of $P_2(t)$ for all vectors in the 10-mer bulk system is shown in Fig. 9a. The dynamics of the two backbone vectors is indistinguishable and from now on we only discuss $\mathbf{v}^{\text{bb b}}$. As expected, the backbone dynamics is slower than the dynamics of the phenyl groups, which are less constrained. The two phenyl group vectors also have different dynamical behaviour, with the vector attached to the backbone, $\mathbf{v}^{\text{ph b}}$, being slower than $\mathbf{v}^{\text{ph p}}$. Again, this is to be expected since the phenyl ring can spin/vibrate around the vector $\mathbf{v}^{\text{ph p}}$, whereas $\mathbf{v}^{\text{ph b}}$ is constrained by the motion of the backbone. All the ACFs for bulk PS decorrelate around 10 ns.[§]

Fig. 9b and c show the ACFs for the various systems for vectors $\mathbf{v}^{\text{ph p}}$ and $\mathbf{v}^{\text{bb b}}$. For both vectors the trend is the same: increasing confinement slows the dynamics of the system. The dynamics of S4 is closest to the bulk dynamics but appears to reach a plateau value of around 0.1, which is due to the much slower dynamics of the adsorption layer. For systems S1 and S2 the ACF is almost flat over the whole time range considered here so the system is virtually frozen, which explains the large differences in R_g and R_e seen earlier. Furthermore, it is also clear that the relaxation of the $\mathbf{v}^{\text{bb b}}$ vector is slower than the one of the $\mathbf{v}^{\text{ph p}}$ vector for all systems. The relaxation of the $\mathbf{v}^{\text{ph p}}$ vector is qualitatively similar to that of $\mathbf{v}^{\text{ph b}}$ and is not presented here.

Fig. 9d shows the dynamics of the vector along the monomer backbone, $\mathbf{v}^{\text{bb b}}$, in the bulk system and for the first adsorption layer (regime labelled I in Fig. 5) in systems S1–S4. The atoms (or molecules) have been analyzed for a specific region only for the time they were in it. Note that in the first adsorption layer the dynamics are slow and the segments remain inside this layer for almost the entire simulation time. All confined films show a marked slowing down of the dynamics, compared to the bulk one, and none of the adsorption layers in any of the thin film systems decorrelate over a time of 100 ns. This is clear evidence

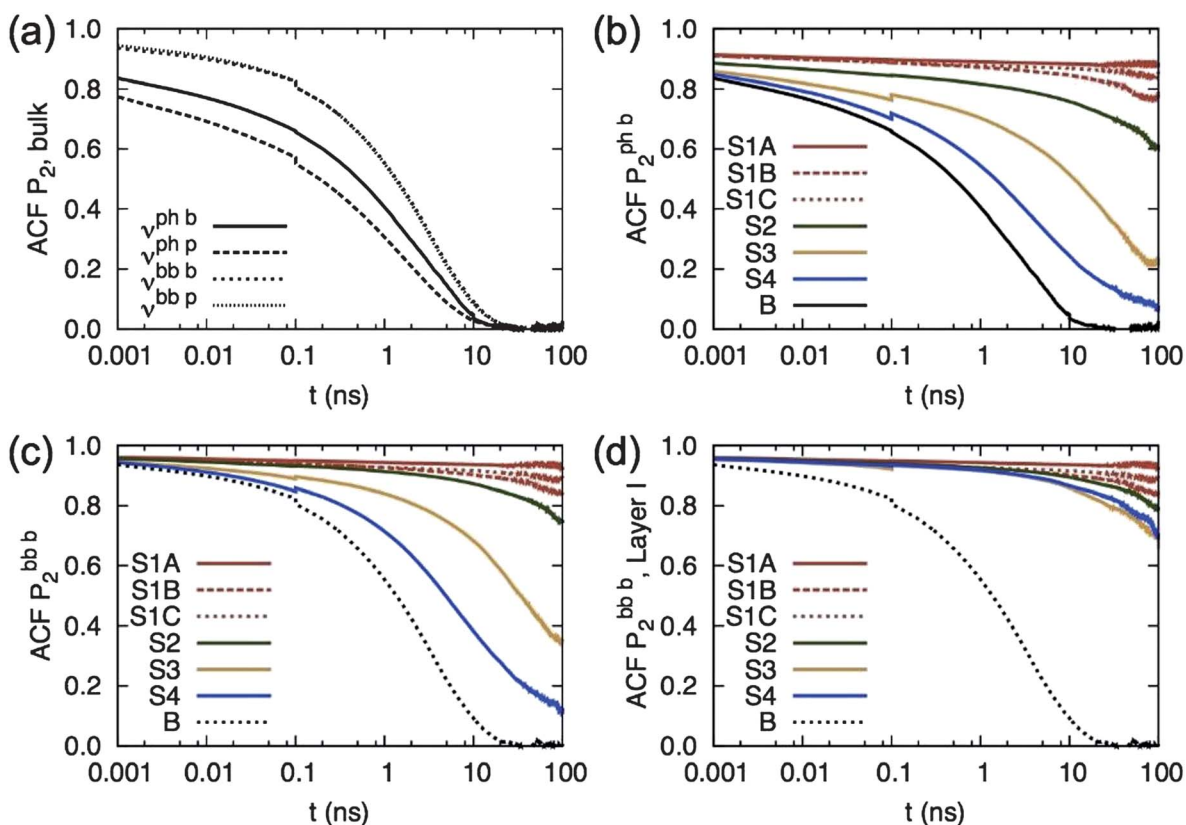


Fig. 9 (a) Time autocorrelation function of P_2 in bulk for all the vectors shown in Fig. 6. (b) The ACF of $\mathbf{v}^{\text{ph } b}$ for all systems. The ACF of $\mathbf{v}^{\text{ph } p}$ is qualitatively similar. (c) The ACF of $\mathbf{v}^{\text{bb } b}$ for all systems. (d) The ACF of $\mathbf{v}^{\text{bb } b}$ for the adsorption layer in all systems.

of the strong influence of the Au surface on the polymer atoms close to it.

To obtain quantitative information about the segmental relaxation time from the ACFs discussed above we fit the $P_2(t)$ data with stretched exponential Kohlrausch–Williams–Watts (KWW) functions⁵⁹ of the form

$$P_2(t) = A \exp \left[- \left(\frac{t}{t_{\text{KWW}}} \right)^\beta \right] \quad (6)$$

where t_{KWW} is the relaxation time and β is the stretch exponent accounting for deviation from the ideal Debye behaviour.[‡] A is a pre-exponential factor that takes into account relaxation processes (such as bond and angle vibrations) at very short time scales. The curves of Fig. 9 can be fitted with the above KWW function for time scales up to a few ns after which the data reach the plateau value, or to about 20 ns when the data becomes too noisy. The segmental relaxation times and the stretching exponents for the various layers in each system are presented in Table 7 for $\mathbf{v}^{\text{bb } b}$, $\mathbf{v}^{\text{ph } p}$ and $\mathbf{v}^{\text{ph } b}$. As we can see t_{KWW} of all three vectors exhibit qualitatively the same behavior. In more detail, the dynamics of the most strongly confined systems, S1, as well as the S2 systems, is extremely slow, the systems are practically frozen.

[‡] For a system with independence of molecular rotation and translation and rotational motions described by the rotational diffusion equation, $\beta = 1$ (see Chapter 7 of ref. 60).

The first adsorption layer of the S3 and S4 systems exhibits a very slow relaxation with a characteristic relaxation time around two orders of magnitude larger than for the bulk system. The second regime (labelled II in Fig. 5) for these systems shows a much faster dynamics than the first adsorption layer with its relaxation time of $\mathbf{v}^{\text{ph } p}$ being about 6 times slower than for the bulk case and 12–16 times slower than bulk for $\mathbf{v}^{\text{ph } b}$ and $\mathbf{v}^{\text{bb } b}$. Finally, the third and fourth regimes for the largest film (S4 system) are characterized by relaxation times that are 2–3 times longer than the bulk system. Values of the stretch exponent β for the $\mathbf{v}^{\text{bb } b}$ vector are in the range between 0.2–0.6 exhibiting a broad distribution of relaxation times. Furthermore, two additional points are observed: (a) First, for both confined and bulk systems the values of β of the different vectors are very close to each other with the data for the $\mathbf{v}^{\text{ph } p}$ one being slightly smaller; *i.e.* a vector along the phenyl ring exhibits a broader distribution of relaxation times than a vector along the backbone. This is in agreement with recent simulation and experimental data of a higher molecular weight bulk PS system.⁶¹ (b) Second, for all vectors the values of β for the molecules belonging in the first adsorbed layer are smaller than that for the ones in the bulk-like region (and in the bulk systems), showing that the confinement results in a broader distribution of segmental relaxation times. We should also note here that the above behaviour is qualitatively similar to the one observed for linear polymers, such as polyethylene close to a graphite surface,²³ where it was observed that the local dynamics of the atoms in only the first adsorption layer were

affected by the surface. In the present case the influence extends over a slightly larger length scale because of two reasons: (a) a much stronger molecule–surface interaction potential, and (b) due to the presence of bulky (phenyl) side groups.

In the final part we consider the analysis of the translational dynamics of the confined PS short chains by calculating the mean square displacements (MSDs) of the monomer centers-of-mass. The results of this analysis are shown in Fig. 10a. The bulk, as well as the two bigger systems (S3 and S4) exhibit, as expected, non-linear anomalous dynamics for short times (up to about 1 ns), and linear Fickian dynamics at longer times. The behaviour of the two smaller, more confined systems, is very different. Both S1 and S2 systems are practically frozen, *i.e.* there are only small vibrations and rotations (see Fig. 10a), of about 0.2 nm for S1 and 0.3 nm for S2.

To determine the dynamics in the different adsorption layers the MSDs along xy have been analysed in slices divided by planes

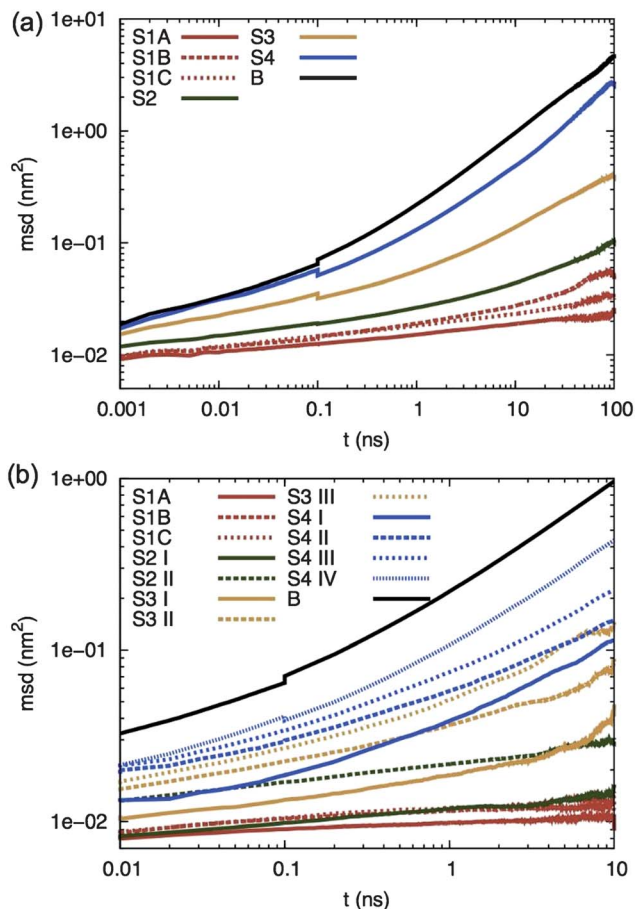


Fig. 10 Translational centre-of-mass dynamics of all confined PS systems studied here: (a) mean square displacements of monomer centres-of-mass (b) mean square displacements along xy of monomer centres-of-mass in the various adsorption layers.

§ The small discontinuities in the graphs at around 0.1 ns are due to the statistical analysis of the data. However, they do not significantly affect the fitting process or derived relaxation times presented in Table 7.

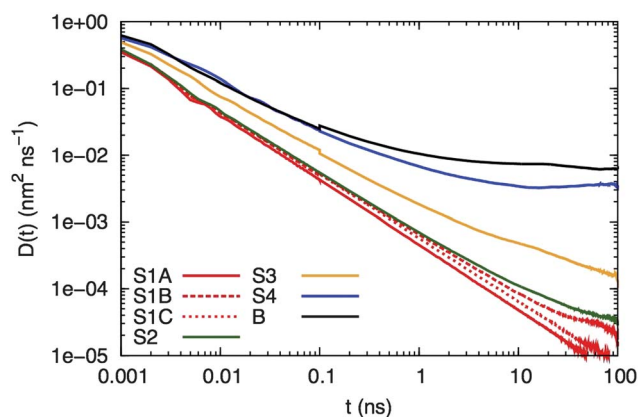


Fig. 11 Diffusion of the chain centres-of-mass.

parallel to the surface, corresponding to the regions shown in Fig. 5. As before, the atoms (or molecules) have been analyzed for a specific region only for the time they were in it. The S4 system has been divided into four regions *i.e.* three layers at each surface and a bulk-like phase in the middle (labelled IV) whereas the S1 systems have only one region (two symmetric adsorption layers). The values of the MSDs for all the systems and the various regimes studied here are plotted in Fig. 10b. After a few ns the data is rather noisy due to the fact that the sample size in the adsorption layers is smaller than for the entire film. First, it is clear that the layers closest to the surface in each case, labelled I, are significantly slower than the more central layers. The dynamics of the adsorption layers in S2 is similar than in S1. However, the dynamics of the adsorption layer in systems S3 and S4 is faster than for systems S1 and S2, with S4 being the fastest. In both S3 and S4 it is clear that the dynamics is faster in the more central layers and S4's middle layer, labelled IV, is closest to the bulk dynamics.

The qualitatively different behaviour between the films is even clearer if we calculate the time-dependent self-diffusion coefficient, defined as

Table 7 Segmental relaxation times t_{KWW} (in ns) and stretching exponents β for the vectors $\mathbf{v}^{ph p}$, $\mathbf{v}^{ph b}$ and $\mathbf{v}^{bb b}$ in the different adsorption layers. The error bars for t_{KWW} are about 30% of the actual value and for the stretching exponents about 0.05–0.1 in all cases

Film	Region	$\mathbf{v}^{ph p}$		$\mathbf{v}^{ph b}$		$\mathbf{v}^{bb b}$	
		t_{KWW}	β	t_{KWW}	β	t_{KWW}	β
S1A	I	$\sim 7 \times 10^4$	0.20	$\sim 10^7$	0.27	$> 10^8$	0.27
S1B	I	$\sim 2 \times 10^4$	0.22	$\sim 10^7$	0.26	$> 10^8$	0.25
S1C	I	$\sim 3 \times 10^4$	0.25	$\sim 10^7$	0.27	$> 10^8$	0.28
S2	I	350.0	0.29	3.0×10^3	0.35	6.0×10^3	0.40
S2	II	200.0	0.30	0.7×10^3	0.35	2.0×10^3	0.40
S3	I	105.0	0.30	600.0	0.36	10^3	0.50
S3	II	18.5	0.35	29.0	0.44	64.0	0.55
S3	III	7.0	0.40	11.0	0.48	25.0	0.58
S4	I	35.0	0.36	100.0	0.40	620.0	0.53
S4	II	5.5	0.38	20.0	0.40	40.0	0.58
S4	III	3.2	0.47	4.3	0.48	9.0	0.57
S4	IV	1.8	0.52	2.2	0.55	4.8	0.60
B		0.9	0.50	1.6	0.60	2.5	0.61

$$D(t) = \frac{\langle (R(t) - R(0))^2 \rangle}{6t},$$

where R is the position of the chain center-of-mass. The diffusion for each film is shown in Fig. 11.‡ As expected, the bulk system shows a time dependent value for the short times whereas it reaches a plateau value (at around 10–50 ns) of $\approx 6 \times 10^{-3} \text{ nm}^2 \text{ ns}^{-1}$. The thickest films (S4) exhibits qualitatively similar behaviour with a plateau, time-independent, value of $\approx 3 \times 10^{-3} \text{ nm}^2 \text{ ns}^{-1}$. The molecules in the S3, S2 and S1 systems, however, show a constantly decreasing $D(t)$, which is to be expected since the molecules in these systems are practically frozen.

4 Summary and conclusions

This research is a hierarchical dualscale study of short PS (10mer) chains confined between two gold surfaces at $T = 503 \text{ K}$ and $P = 1 \text{ atm}$. A combination of DFT calculations and MD simulations were used. The DFT data were used to develop an accurate classical atomistic potential for the polymer with the surface. This interfacial potential was used in MD simulations for PS thin films confined between two parallel gold surfaces.

To obtain detailed chemical information at the interface, DFT calculations of ethane (representing the polymer backbone) adsorbed at different sites on the Au(111) surface were performed. The DFT calculations show that the adsorption of ethane on the gold surface is almost entirely due to vdW forces. The adsorption energies on the various surface sites and different molecular orientations were examined and the minimum energy configuration is for ethane to lie with its C–C bond parallel to the surface. The corresponding adsorption energy is $-35.7 \text{ kJ mol}^{-1}$.

The derivation of a new, accurate classical pair molecule–surface force field, through parameterization of detailed DFT data, is a major part of this work. Using an optimization algorithm based on simulated annealing, we obtained a set of non-bonded pair C–Au and H–Au parameters for ethane (the PS backbone) that accurately describe the detailed DFT data. We found that a Morse-type potential is a better choice than a Lennard-Jones potential for describing the DFT data. The Morse potential parameterisations give good agreement between the DFT and classical data for both flat and vertical molecular orientations. The potential for the phenyl group was developed in the same way in a previous publication.³²

These interfacial potentials are used to describe the interaction between PS and gold in *NPT* molecular dynamics simulations. Four systems with different numbers of polystyrene oligomers were studied using detailed all-atom molecular dynamics simulations. The PS film thicknesses ranged from 0.96–9.5 nm. For the thinnest system, three independent films were simulated in order to study the difference in the initial conditions in the preparation of the model systems. The density, structure and dynamics of the PS films were analysed. The radius of gyration and end-to-end distance of the chains show that only the chains in the thinnest films (S1) exhibit a different conformation than in bulk PS.

All films have a density peak, or adsorption layer, in the PS film at the gold surface, which is 2.5–3 times higher than the bulk density. For longer distances the density reaches already a plateau value similar to the average bulk density. An analysis of

the conformation tensor shows that the chains in the adsorption layer tend to lie along the surface. Similarly, an analysis of the bond order parameter P_2 showed that the phenyl and the backbone rings in the adsorption layer prefer to orient parallel to the surface. The S3 and S4 systems show a weak second adsorption layer but no strong orientation ordering was found in this layer. The density reaches a constant bulk value of around 1.5–2 nm from the surface and the bond order parameters and conformation tensor components return to a bulk value at around the same distance, which is of the order of R_e or 2–3 times R_g .

For the three thinnest (S1) films the average end-to-end chain length was found to be smaller than for the other systems with average values ranging from 1.31–1.41 nm, compared to the bulk value of 1.54 nm. The average radius of gyration is also slightly smaller in these films. In this highly confined system (average film thickness of about 0.6 times the average end-to-end distance) the PS chains are practically trapped in a metastable configuration that depends strongly on the preparation of the model systems (history of the samples).

The time autocorrelation function of P_2 shows that the thinner the film the more the dynamics is suppressed. At 503 K, the central part of the 10 nm film (S4) is only slightly affected by the interfaces and approaches bulk-like dynamics. Close to the interface, in the first adsorption layer, the dynamics is slower by up to 1–2 orders of magnitude. For thinner films, this central, almost bulk-like layer disappears and for the thinnest films the polymer feels a strong influence from both the top and bottom surfaces, which effectively freezes the polymer film. For all films, the autocorrelation function does not completely decorrelate, which is due to the slower dynamics in the first adsorption layer. A quantitative analysis of the relaxation times show a clear influence on the monomer orientational relaxation for distances up to the second adsorption layer, about 1–2 nm.

Due to the slow dynamics at the surface, studies of polymer–solid systems are computationally challenging at the atomistic level due to the long time scales required for equilibration. Therefore, future work will be the development of a rigorous CG model for the polymer–surface interaction. This could then be used to study systems with higher molecular weights and the effect of confinement on the glass transition temperature.

Acknowledgements

The authors would like to thank Kostas Daoulas, Dominik Fritz and Kurt Kremer for valuable discussions and critical reading of the manuscript. Funding was provided by the DFG SPP 1369 Priority Program. Partially supported by the European Union's Seventh Framework Programme (FP7-REGPOT-2009-1) project "Archimedes Center for Modeling, Analysis and Computation" under grant agreement n 245749.

References

- 1 R. D. Priestley, C. J. Ellison, L. J. Broadbelt and J. M. Torkelson, *Science*, 2005, **309**, 456.
- 2 S. Anastasiadis, K. Karatasos, G. Vlachos, E. Manias and E. P. Giannelis, *Phys. Rev. Lett.*, 2000, **84**, 915.
- 3 K. F. Mansfield and D. N. Theodorou, *Macromolecules*, 1989, **22**, 3143.
- 4 K. F. Mansfield and D. N. Theodorou, *Macromolecules*, 1991, **24**, 4295.

- 5 S. K. Kumar, M. Vacatello and D. Y. Yoon, *J. Chem. Phys.*, 1988, **89**, 5206.
- 6 I. A. Bitsanis and G. Hatzioannou, *J. Chem. Phys.*, 1990, **92**, 3827.
- 7 Jörg Baschnagel and Kurt Binder, *Macromolecules*, 1995, **28**, 6808.
- 8 T. K. Xia, J. Ouyang, M. W. Ribarsky and U. Landman, *Phys. Rev. Lett.*, 1992, **69**, 1967.
- 9 T. C. Clancy and W. L. Mattice, *Comput. Theor. Polym. Sci.*, 1999, **9**, 261.
- 10 D. B. Zax, D.-K. Yang, R. A. Santos, H. Hegemann, E. P. Giannelis and E. Manias, *J. Chem. Phys.*, 2000, **112**, 2945.
- 11 T. Matsuda, G. D. Smith, R. G. Winkler and D. Y. Yoon, *Macromolecules*, 1995, **28**, 165.
- 12 P. C. Mischler, J. Baschnagel, S. Dasgupta and K. Binder, *Polymer*, 2002, **43**, 467.
- 13 T. Ayoagi, J. Takimoto and M. Doi, *J. Chem. Phys.*, 2001, **115**, 552.
- 14 J. L. Keddie, R. A. L. Jones and R. A. Cory, *Europhys. Lett.*, 1994, **27**, 59–64.
- 15 J. L. Keddie, R. A. L. Jones and R. A. Cory, *Faraday Discuss.*, 1994, **98**, 219–230.
- 16 E. P. Giannelis, R. Krishnamoorti and E. Manias, *Adv. Polym. Sci.*, 1999, **138**, 107.
- 17 K. Fukao and Y. Miyamoto, *Phys. Rev. E: Stat. Phys., Plasmas, Fluids, Relat. Interdiscip. Top.*, 2000, **61**, 1743.
- 18 L. Singh, P. J. Ludovice and C. L. Henderson, *Thin Solid Films*, 2004, **449**, 231.
- 19 C. J. Ellison, M. K. Mundra and J. M. Torkelson, *Macromolecules*, 2005, **38**, 1767.
- 20 M. Y. Efremov, E. A. Olson, M. Zhang, Z. Zhang and L. H. Allen, *Phys. Rev. Lett.*, 2003, **91**, 085703.
- 21 M. Tress, M. Erber, E. U. Mapesa, H. Huth, J. Mueller, A. Sergei, christpph Schick, K.-J. Eichhorn, B. Voit and F. Kremer, *Macromolecules*, 2010, **43**, 9937.
- 22 W. E. Wallace, J. H. van Zanten and W. L. Wu, *Phys. Rev. E*, 1995, **52**, R3329.
- 23 V. A. Harmandaris, K. C. Daoulas and V. G. Mavrantzas, *Macromolecules*, 2005, **38**, 5796.
- 24 S. Peter, S. Napolitano, H. Meyer, M. Wübbenhorst and J. Baschnagel, *Macromolecules*, 2008, **41**, 7729–7743.
- 25 L. Yelash, P. Virnau, K. Binder and W. Paul, *Phys. Rev. E*, 2010, **82**, 050801.
- 26 K. Johnston, R. M. Nieminen and K. Kremer, *Soft Matter*, 2011, **7**, 6457–6466.
- 27 A. R. C. Baljon, S. Williams, N. K. Balabaev, F. Paans, D. Hudzinskyy and A. V. Lyulin, *J. Polym. Sci., Part B: Polym. Phys.*, 2010, **48**, 1160.
- 28 D. Hudzinskyy, A. V. Lyulin, A. R. C. Baljon, N. K. Balabaev and M. A. J. Michels, *Macromolecules*, 2011, **44**, 2299.
- 29 M. L. Sushko, A. Y. Gal and A. L. Shluger, *J. Phys. Chem. B*, 2006, **110**, 4853.
- 30 O. Borodin, G. D. Smith, R. Bandyopadhyaya and O. Bytner, *Macromolecules*, 2003, **36**, 7873.
- 31 L. Delle Site, C. F. Abrams, A. Alavi and K. Kremer, *Phys. Rev. Lett.*, 2002, **89**, 156103.
- 32 K. Johnston and V. Harmandaris, *J. Phys. Chem. C*, 2011, **115**, 14707.
- 33 G. Kresse and J. Hafner, *Phys. Rev. B*, 1993, **47**, 558.
- 34 G. Kresse and J. Hafner, *Phys. Rev. B*, 1994, **49**, 14251.
- 35 G. Kresse and J. Furthmüller, *Comput. Mater. Sci.*, 1996, **6**, 15.
- 36 G. Kresse and J. Furthmüller, *Phys. Rev. B*, 1996, **54**, 11169.
- 37 P. E. Blöchl, *Phys. Rev. B*, 1994, **50**, 17953.
- 38 G. Kresse and D. Joubert, *Phys. Rev. B*, 1999, **59**, 1758.
- 39 M. Dion, H. Rydberg, E. Schröder, D. C. Langreth and B. I. Lundqvist, *Phys. Rev. Lett.*, 2004, **92**, 246401.
- 40 M. Dion, H. Rydberg, E. Schröder, D. C. Langreth and B. I. Lundqvist, *Phys. Rev. Lett.*, 2005, **95**, 109902(E).
- 41 A. Gulans, M. J. Puska and R. M. Nieminen, *Phys. Rev. B*, 2009, **79**, 201105(R).
- 42 J. P. Perdew, K. Burke and M. Ernzerhof, *Phys. Rev. Lett.*, 1996, **77**, 3865.
- 43 J. Perdew, K. Burke and M. Ernzerhof, *Phys. Rev. Lett.*, 1997, **78**, 1396.
- 44 H. Berendsen, D. van der Spoel and R. van Drunen, *Comput. Phys. Commun.*, 1995, **91**, 43.
- 45 E. Lindahl, B. Hess and D. van der Spoel, *J. Mol. Model.*, 2001, **7**, 306.
- 46 B. Hess, C. Kutzner, D. van der Spoel and E. Lindahl, *J. Chem. Theory Comput.*, 2008, **4**, 435–447.
- 47 G. Bussi, D. Donadio and M. Parinello, *J. Chem. Phys.*, 2007, **126**, 014101.
- 48 B. N. Dutta and B. Dayal, *Phys. Status Solidi B*, 1963, **3**, 473.
- 49 K. C. Daoulas, V. A. Harmandaris and V. G. Mavrantzas, *Macromolecules*, 2005, **38**, 5780.
- 50 F. Müller-Plathe, *Macromolecules*, 1996, **29**, 4782.
- 51 T. G. Fox and P. J. Flory, *J. Polym. Sci.*, 1954, **14**, 315–319.
- 52 P. Claudy, J. M. Letoffe, Y. Camberlain and J. P. Pascault, *Polym. Bull.*, 1983, **9**, 208–215.
- 53 P. G. Santangelo and C. M. Roland, *Macromolecules*, 1998, **31**, 4581–4585.
- 54 S. D. Chakarova-Käck, E. Schröder, B. I. Lundqvist and D. C. Langreth, *Phys. Rev. Lett.*, 2006, **96**, 146107.
- 55 S. M. Wetterer, D. J. Lavrich, T. Cummings, S. L. Bernasek and G. Scoles, *J. Phys. Chem. B*, 1998, **102**, 9266.
- 56 S. Piana and A. Bilic, *J. Phys. Chem. B*, 2006, **110**, 23470.
- 57 T. V. M. Nodoro, E. Voyiatzis, A. Ghanbari, D. N. Theodorou, M. C. Böhm and F. Müller-Plathe, *Macromolecules*, 2011, **44**, 2316.
- 58 S. K. Kumar, M. Vacatello and D. Y. Yoon, *Macromolecules*, 1990, **23**, 2189.
- 59 G. Williams and D. C. Watts, *Trans. Faraday Soc.*, 1970, **66**, 80.
- 60 B. J. Berne and R. Pecora, *Dynamic light scattering: with applications to chemistry, biology, and physics*, 2000.
- 61 V. Harmandaris, G. Floudas and K. Kremer, *Macromolecules*, 2011, **44**, 393.